Journal Pre-proofs

Correlation of Early-Stage Growth Process Conditions with Dislocation Evolution in MOCVD-Based GaP/Si Heteroepitaxy

J.T. Boyer, A.N. Blumer, Z.H. Blumer, D.L. Lepkowski, T.J. Grassman

PII: S0022-0248(21)00226-8
DOI: https://doi.org/10.1016/j.jcrysgro.2021.126251
Reference: CRYS 126251

To appear in: *Journal of Crystal Growth*

Received Date: 25 March 2021
Revised Date: 10 June 2021
Accepted Date: 9 July 2021

Please cite this article as: J.T. Boyer, A.N. Blumer, Z.H. Blumer, D.L. Lepkowski, T.J. Grassman, Correlation of Early-Stage Growth Process Conditions with Dislocation Evolution in MOCVD-Based GaP/Si Heteroepitaxy, *Journal of Crystal Growth* (2021), doi: https://doi.org/10.1016/j.jcrysgro.2021.126251

Correlation of Early-Stage Growth Process Conditions with Dislocation Evolution in MOCVD-Based GaP/Si Heteroepitaxy

J. T. Boyer,[1] A. N. Blumer,[1,2] Z. H. Blumer,[1] D. L. Lepkowski,[3] and T. J. Grassman[1,2,3]

[1] *Department of Materials Science and Engineering, The Ohio State University, Columbus, OH 43210, USA*
[2] *Center for Electron Microscopy and Analysis, The Ohio State University, Columbus, OH 43212, USA*
[3] *Department of Electrical and Computer Engineering, The Ohio State University, Columbus, OH 43210, USA*

To identify the complex relationships between early-stage growth processes and the resultant defect microstructure in GaP/Si heteroepitaxy, a holistic study of several key metal-organic chemical vapor deposition (MOCVD) parameters was conducted, focusing on Si surface preparation and GaP atomic layer epitaxy (ALE) based nucleation processes. Crystalline defects related to the lattice mismatch and/or interfacial heterovalency, namely misfit dislocations (MD), threading dislocations (TD), and stacking fault pyramids (SFP), were quantitatively characterized via electron channeling contrast imaging (ECCI) and correlated against the different process variations. Choice of Si surface preparation method between the two examined (dilute SiH_4 annealing versus Si_2H_6 based homoepitaxy) had little impact on resultant GaP film morphology and defect content, whereas differing GaP ALE nucleation conditions produced much more substantial changes. In particular, the initial precursor species (*tert*-butylphosphine versus triethygallium) and ALE cycle purge times both yielded significant influence over threading dislocation densities (TDD) in thin (100 nm), post-critical thickness GaP/Si films, with TDD spanning two orders of magnitude, from 6.7×10^7 cm^{-2} to 7.1×10^5 cm^{-2}, depending on the specific process conditions employed. SFP densities were also found to follow a similar trend, ranging from 2.0×10^7 cm^{-2} to 1.8×10^5 cm^{-2}, but with no apparent causal relationship between SFP density and TDD. To help explain the dramatic differences observed, detailed, large-area MD network characterization was used to provide statistically-relevant quantitative analyses of the critical dislocation dynamics (introduction rates and glide velocities) associated with the different process variants. These extracted values are then correlated against the ALE process variants to provide insight into the potential mechanistic roles of the different growth processes.

I. INTRODUCTION

Development of epitaxially-integrated III-V/Si materials is strongly motivated by the potential expansion of the integrated (opto)electronic device design palette. The combination of tunable electronic and photonic functionalities afforded by the III-V alloys with the ubiquitous Si microelectronics platform can enable a considerable degree of flexibility that promises to usher in a new era of semiconductor technologies. Advances in III-V/Si can be transferred to photovoltaic, optoelectronic, and photonic-integrated circuitry fields, thereby adding improved functionality and/or cost reduction to energy production, communication, and computing industries.

To meet the performance needs of most devices based on cubic III-V semiconductors [1]–[3], low threading dislocation density (TDD) must be achieved within the integrated III-V layers, which are almost universally lattice-mismatched versus Si. The binary (i.e. simplest) III-V material most conveniently situated to serve as a direct epitaxial integration bridge between the Si and subsequent cubic III-V epilayers is GaP, with a room temperature compressive misfit of only -0.36%. Although the lattice mismatch of subsequent III-V layers can be controlled by means of composition, such as with graded buffers, the GaP/Si mismatch is both unavoidable and increases at growth temperature due to mismatched rates of thermal expansion.

Because this is the first misfit interface within any such epitaxial structure, control of the resultant dislocation populations (i.e. minimization of TDD) within GaP/Si is critical. In general, this means maximizing the length (via glide of threading segments [4]) of any associated strain-relieving misfit dislocations (MDs) present at the GaP/Si interface [5] and minimizing the total amount of dislocation introduction [6], [7].

The heterovalent GaP/Si integration system has received considerable investigation for decades. A wide range of growth methods have been considered, including hydride vapor phase epitaxy [8], molecular beam epitaxy (MBE) [9]–[11], and metal-organic chemical vapor deposition (MOCVD) [12]–[16]. Many of these investigations have demonstrated use of a two-step growth process, consisting of a low temperature nucleation layer [8], [15], commonly via pulsed/cycled precursor delivery processes that force a 2D layer-by-layer growth mode [9], [10], [12], [13], [16]–[18], followed by higher temperature overgrowth using typical bulk-like conditions [12], [19]. To date, the majority of this GaP/Si research has centered on eliminating nucleation-related defects [9]–[15] ─ antiphase domains (APDs), stacking faults (SFs), and microtwins (MTs), which themselves are believed to serve as likely dislocation generation and/or multiplication sources — thereby rendering possible more recent work focused solely on achieving low TDD [20]. However, as of yet, there is little in the way of understanding about the impact of the nucleation processes themselves and the evolution of the eventual misfit dislocations.

One early MBE-based study that did touch on this topic used transmission electron microscopy (TEM), in both plan-view (PVTEM) and cross-section (XTEM) geometries, to show that the use of a 2D layer-by-layer nucleation process, migration enhanced epitaxy (MEE), yielded longer MDs and fewer TDs, as well as fewer SFs [9], than the more 3D prone conventional co-evaporation process. However, while TEM provides excellent resolution of such defect structures [7], [9], its statistical relevance is limited by the relatively small analysis areas (generally <100 μm^2). This small of an analysis window provides little insight into MD evolution when such structures are expected to extend by 100's or 1000's of μm [5], [21]–[23]. More recent work, using metal-organic chemical vapor deposition (MOCVD) growth and its MEE equivalent, atomic layer epitaxy (ALE), as well as a more statistically relevant characterization approach based on electron channeling contrast imaging (ECCI), found a correlation between stacking fault pyramid (SFP) populations and ALE cycle counts [24]. Furthermore, interactions between SFPs and MDs were observed, and a causal relationship between SFP density and elevated TDD was suggested.

Nonetheless, due to the narrow scope of process conditions and characterization in these, and indeed most reports on GaP/Si growth, and given the compounding problems of heterovalent (polar/non-polar) behavior [11], [25]–[27] with nucleation related defects [9]–[15] and lattice mismatch [27] at this interface, there is as yet insufficient insight into the broader relationships of process conditions, interface chemistry, nucleation defects, and MD evolution within GaP/Si. Understanding the impact of the nucleation process itself on the evolution of the eventual dislocation microstructure is still needed to enable true epitaxial flexibility and scalability necessary for continued development of associated III-V/Si technologies.

To this end, the work reported here examines a somewhat wider, systematic array of MOCVD GaP/Si nucleation process conditions and endeavors to clearly correlate them with the resultant defect structures and populations, focusing on the resultant MD networks and terminal TDD. To ensure statistical relevance and reproducibility of the collected data, accurate quantitative analysis was employed via large-area, defect-resolved ECCI based characterization of numerous as-grown heteroepitaxial structures [28]–[31]. Figure 1 provides a schematic process-structure relation diagram that captures the organizational approach of this effort (and its presentation herein).

Multiple aspects of the overall GaP/Si MOCVD process flow — specifically as related to the GaP nucleation, including Si substrate pretreatment method, choice of ALE initiation precursor species, and ALE cycle/purge timing — were systematically studied as independent variables. Use of dedicated GaP/Si samples grown to 100 nm film thickness, or ~2× beyond the critical thickness [28], [32], enabled analysis of the early stage microstructure. The

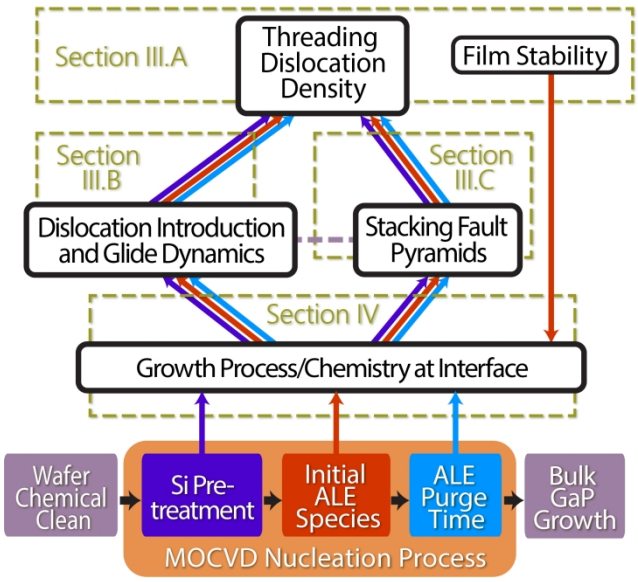

Figure 1: Schematic outline of the MOCVD GaP/Si growth process flow and associated linkages to process-structure relationships explored in this study (and the section where they are discussed).

effect of each of the process variants was quantitatively correlated with TDD as the primary outcome of interest, but also with secondary results of MD network morphology/evolution and SFP populations.

Across the range of samples examined, the resultant TDD in the 100 nm GaP/Si was found to span nearly two orders of magnitude, down to as low as 7×10^5 cm^{-2}, with a systematic dependence on the process parameters used. Going further, metrics related to the underlying dislocation dynamics (i.e. introduction rate and glide velocity) were extracted and are compared between the variants that had the strongest impact on TDD. Lastly, potential mechanisms behind the observed MD network evolution are discussed, with consideration of intermediate factors, like SFP populations and interfacial chemistries.

II. METHODS

A. Growth Processes

All GaP/Si samples reported herein were grown in a 3 × 2" Aixtron close-coupled showerhead MOCVD system. Precursors used for the growths were silane (SiH_4), disilane (Si_2H_6), triethylgallium ($C_6H_{15}Ga$, "TEGa"), and *tert*-butylphosphine ($C_4H_{11}P$, "TBP"), with H_2 as the carrier gas. Total gas flow was maintained at 6 slm under a total reactor pressure of 150 mbar. A LayTec epiTT reflectance/pyrometry system provided *in situ* monitoring during growths.

The general MOCVD GaP/Si nucleation and growth process flow is outlined at the bottom of Figure 1, highlighting the three key parameters/variables considered herein: Si pretreatment, initial ALE species, and ALE purge time. A total of five distinct sample variants based on combinations of the aforementioned process variables, summarized in Table 1 as Processes A – E, were produced to systematically study the effect of each aspect of the nucleation process. Multiple samples were produced within each category to ensure reproducibility and minimize the impact of any run-to-run inconsistencies.

The epi-ready Si wafers used in this work were (001)-oriented with intentional offcut ranging 2° – 6° toward [110]. All wafers underwent a chemical cleaning process consisting of 3:1 H_2SO_4:H_2O_2 piranha etch followed by an HF-last de-oxidation and passivation etch immediately prior to loading into the MOCVD reactor. The "Si pretreatment" step was then used to prepare a pristine, double-height stepped Si surface; this was the first key process parameter investigated. Two different Si pretreatment processes were considered: growth of a 90 nm thick, not intentionally doped, homoepitaxial Si layer at 760°C using Si_2H_6 ("Si_2H_6 epitaxy"), similar to other reports [12], [13], versus annealing at 750 – 800°C under dilute SiH_4 flow ("SiH_4 anneal"), with no appreciable Si growth, similar to methods reported in [33].

Following Si pretreatment, the substrate was cooled to ~450°C in preparation for ALE. The ALE TEGa dose (pulse time × molar flow) was calibrated to yield a single monolayer of Ga over 2 sec, based on the GaP growth rate at 450°C. Separate testing of thin ALE layers determined that this TEGa dose led to a minimum surface roughness, as measured via atomic force microscopy (AFM). The TBP pulses were set to provide an effective V:III molar dose ratio of 95, except in the case of the TBP-initiated process, where a 5× longer TBP pulse was used at

Table 1: Details of the five process variants in this work and overall TDD resulting from each.

	Process A	Process B	Process C	Process D	Process E
Si Pretreatment	SiH_4 Anneal	SiH_4 Anneal	SiH_4 Anneal	Si_2H_6 Epitaxy	Si_2H_6 Epitaxy
Initial ALE Species	TEGa-Initiated	TEGa-Initiated	TBP-Initiated	TEGa-Initiated	TBP-Initiated
ALE Purge Time	1 sec (short)	10 sec (long)	10 sec (long)	1 sec (short)	10 sec (long)
Total TDD [$\times 10^6$ cm^{-2}]	67.5 ± 9.4	11.7 ± 3.3	1.1 ± 0.1	58.1 ± 11.1	0.7± 0.1

the beginning (on the bare Si). Unless noted otherwise, the full ALE process consisted of 15 total cycles of alternating TEGa and TBP pulses [12], [13], to yield a nominal GaP film thickness of about 4 nm.

In addition to the Si pretreatment, two key variables related to the ALE nucleation process itself were investigated. The first of these, "initial ALE species," considered the impact of the precursor species, TEGa versus TBP, used in the first pulse onto the bare Si. The other major process parameter studied, "ALE purge time," considered the impact of the length of the reactor purge (i.e. pure H_2 flow) in between each precursor pulse. Purge times of 1 sec ('short') and 10 sec ('long') were compared. Unless noted otherwise, all other conditions and process parameters (pulse lengths, total cycles, temperature, pressure) were held constant.

Following the ALE nucleation, the substrate temperature was raised to 625°C under a low TBP flow to stabilize the surface. Bulk growth of GaP at ~0.5 µm/hr and V:III molar flow ratio of 40 was performed to yield a total GaP epilayer thickness of 100 nm. This thickness was determined to be sufficiently beyond the threshold for dislocation introduction and glide (~2× Matthews-Blakeslee critical thickness [32]) to ensure the presence of a representative dislocation population, while still being thin enough to support well-resolved, ECCI-based imaging of defects at the GaP/Si interface. All GaP bulk epilayers were *n*-type doped (via SiH_4) to a target concentration of 1×10^{18} cm^{-3}.

B. Characterization Methods

All epitaxial samples were subjected to a suite of structural characterization methods that enabled rapid feedback. Epilayer surface morphology was analyzed via AFM in a Bruker Icon 3 system. Symmetric (004) and asymmetric (224) high-resolution X-ray diffraction (XRD) reciprocal space maps (RSM) were collected for determination of strain state (i.e. epilayer relaxation) with a Bede D1 triple-axis X-ray diffractometer. Finally, high-accuracy dislocation characterization and quantification was performed using electron channeling contrast imaging (ECCI) in a Thermo Scientific Apreo scanning electron microscope (SEM) outfitted with an annular backscattered electron detector. ECCI provides rapid, non-destructive, large scale defect characterization with one-to-one correspondence to TEM, making it the method of choice for this systematic and quantitative study [29], [34], [35]. All ECCI reported here was performed at an accelerating voltage of 30 kV and beam currents of 1.4 – 6.4 nA. The general ECCI methodology followed that described in our prior reports [28], [29], [36].

For (001)-oriented zincblende GaP under relatively low levels of lattice mismatch, the strain-relieving misfit dislocations preferentially reside within the $\{111\}\langle110\rangle$ slip system, with $\mathbf{b} = \frac{a}{2}\langle110\rangle$ Burgers vectors. Therefore, for enhanced clarity of the MD networks present at the GaP/Si interface, ECCI was conducted using specific $\mathbf{g} = \langle220\rangle$-type diffraction vectors. This approach takes advantage of the standard dislocation contrast (invisibility) criterion, $\mathbf{g} \cdot (\mathbf{b} \times \mathbf{u})$ [37], thereby enabling selective imaging of the two sets of MDs with orthogonal $\mathbf{u} = \langle110\rangle$ line directions. For every sample, both MD sets (line directions) were imaged, but for simplicity only micrographs depicting the $\mathbf{g} = [\bar{2}20]$ diffraction condition, and thus $\mathbf{u} = [110]$ dislocations, are presented in the main document; micrographs depicting the accompanying $\mathbf{g} = [220]$ / $\mathbf{u} = [\bar{1}10]$ sets may be found in the Supplemental, as well as larger ECCI micrographs for all the comparisons shown herein. All micrographs reported herein underwent contrast normalization and light noise reduction to enhance the visibility of features of interest.

In the thin (100 nm) GaP/Si samples studied here, ECCI is highly sensitive to defects within the epilayer all the way down to the interface [29], [38]. As such, the MDs are well-resolved and appear as sharp lines of either bright or dark contrast, depending on their respective Burgers vectors [28]. In this case, the strong MD contrast tends to swamp the weaker contrast TDs, making them difficult to resolve, especially at lower magnifications [28], [39]. Therefore, instead of directly counting TDs, TDD values are estimated from MD endpoint density, based on the fact that there are two TDs associated with every MD, as required by the dislocation loop geometry. As such, "TDD" and "MD endpoint density" are equivalent and used interchangeably.

To provide quantitative metrics for dislocation glide and introduction dynamics, MD arrays of each **u** = ⟨110⟩ direction can be related to the total TDD, ρ_{TD}^{total}, as

$$\rho_{TD}^{total} = \rho_{TD}^{[110]} + \rho_{TD}^{[\bar{1}10]} = \frac{2\rho_{MD}^{[110]}}{L_{MD}^{[110]}} + \frac{2\rho_{MD}^{[\bar{1}10]}}{L_{MD}^{[\bar{1}10]}}, \quad (1)$$

where $\rho_{MD}^{\langle 110\rangle}$ is the average MD linear density, $L_{MD}^{\langle 110\rangle}$ is the average MD length, and $\rho_{TD}^{\langle 110\rangle}$ is the MD endpoint density, or TDD, each resolved per specific indicated direction [5], [7]. Within a given direction, the ensemble average MD length may be simply extracted from the associated TDD and average MD linear density as

$$L_{MD}^{\langle 110\rangle} = \frac{2\rho_{MD}^{\langle 110\rangle}}{\rho_{TD}^{\langle 110\rangle}}. \quad (2)$$

Experimental $\rho_{MD}^{\langle 110\rangle}$ values were obtained via orthogonal line profiles, spaced narrower than the average MD length to ensure adequate sampling. $\rho_{TD}^{\langle 110\rangle}$ and $\rho_{MD}^{\langle 110\rangle}$ were extracted for each sample from at least 10 separate ECCI images of typically 1,000 – 4,000 μm^2 per image, aided by a semi-automated image segmentation procedure, developed in-house and performed with MIPAR image analysis software [30]. The total area imaged per process variant was thus at least 10,000 μm^2 to ensure accurate and representative measurement statistics.

MD lengths can vary greatly, both within a single sample and between samples, and can sometimes be inconveniently long, requiring extremely large micrographs to adequately trace. The approach described above thus simplifies the analysis and avoids sampling inaccuracies associated with direct length measurements. Nonetheless, when needed, direct, ECCI-based MD length measurements can be performed to provide even more detailed information. To capture some of the longest MD lengths encountered, multi-image montages were taken using automated SEM scan-and-stitch software (with human intervention as needed to ensure the diffraction conditions and image quality is maintained throughout). Montages were typically collected to provide long aspect ratios (up to 1:50) in the MD line directions, as needed to capture the full feature length.

III. RESULTS AND ANALYSIS

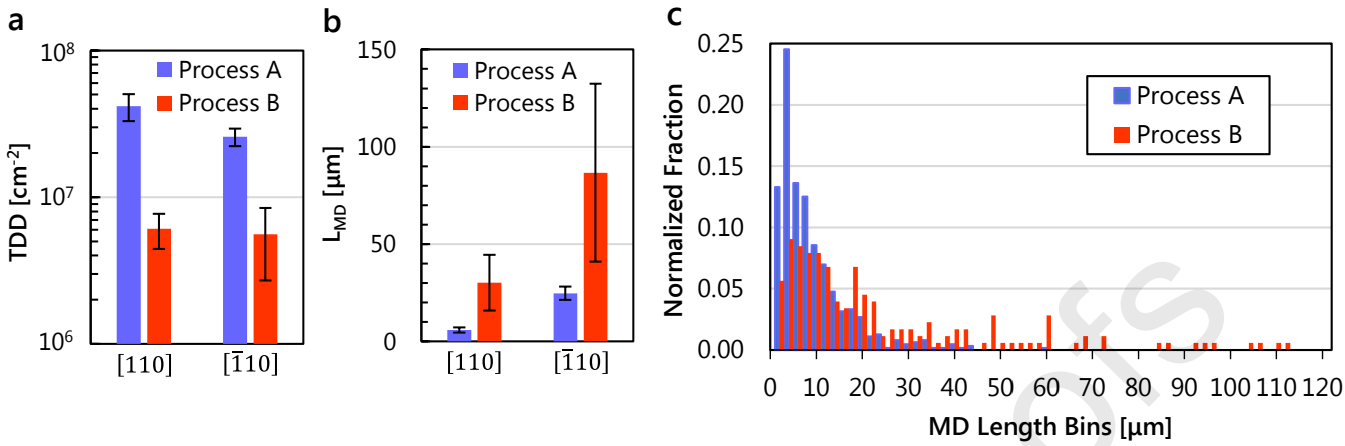

Figure 3: Examination of ALE purge time effects via comparison of Processes A versus B in terms of (a) TDD and (b) average MD length for each MD line direction. (c) Histogram of **u** = [110] MD lengths extracted from ECCI montages. Histogram bins were 2 µm and normalized to the TDD of each process variant to better show the difference in dispersion.

Multiple GaP/Si samples from each category described in Table 1 were produced and thoroughly characterized. As noted previously, some parameter details (wafer offcut and/or SiH_4 anneal temperature) occasionally varied slightly in a non-systematic manner, either intentionally or due to substrate availability. However, no differences in extended defect populations were observed as a result, and thus these details are not discussed herein. All heteroepitaxial GaP/Si films examined exhibited similar surface morphologies and residual strain state. AFM indicated root-mean-square surface roughness (R_q) values of ≤1.2 nm for all samples, unless otherwise noted. No surface-penetrating antiphase domains or borders were observed [40], [41], which is expected due to the use of vicinal substrates and the ALE nucleation process. XRD RSMs indicated partial relaxation in all films, with ~10% and ~5% room-temperature relaxation (or ~3.6×10^{-4} and ~1.8×10^{-4} plastic strain relief) in the [110] and [$\bar{1}$10] directions, respectively. These values are correlated with relaxation calculated from MD arrays in Section III.B.1.

While MD networks were the primary focus of the ECCI-based characterization, stacking fault pyramids (SFPs) were also observed as triangular bow-tie projections (see the inset of Figure 2a), where only the bounding faults that satisfy the contrast criteria of the given g-vector are visible. SFPs are commonly observed in epitaxial films of a variety of zincblende materials (e.g. GaAs [42], GaAs/Ge [43], InGaAs/InP [44], ZnSe/GaAs [45], GaP/Si [24], [28], [46]), where they are commonly linked to imperfections at growth interfaces. The SFPs observed herein generally possessed a maximum edge-to-edge width of ~140 nm, or $\sqrt{2}$ times the GaP film thickness, consistent with the faults lying on {111} planes with the pyramid apex originating at or very near the GaP/Si interface. These features are discussed further in Section III.C.

A. Direct Observation of Process Variable Effects

The most striking and critical trend observed in this work was the two order of magnitude range in total TDD (i.e. sum of MD endpoint density in both line directions), from 7.1×10^5 cm^{-2} to 6.7×10^7 cm^{-2}, across the process variants. The sample categories described in Table 1 enable direct comparisons to help deconvolute the effects of the different process variables. For the sake of clarity, we present these comparisons here in order of simplest to most complex.

1. Impact of ALE Cycle Purge Times

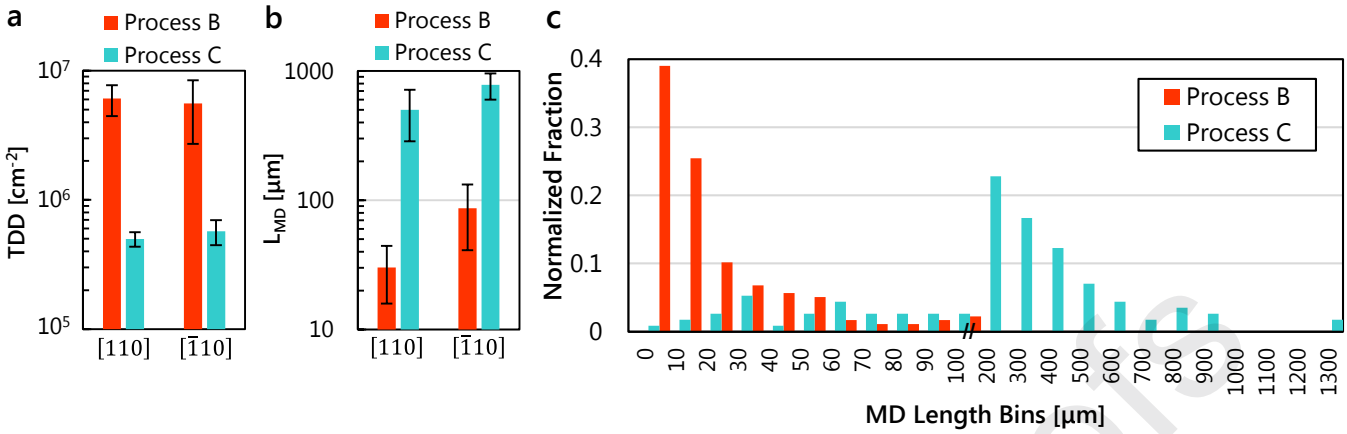

Figure 5: Examination of ALE initiation species effects via comparison of Processes B versus C in terms of (a) overall TDD and (b) average MD length for each MD line direction. (c) Histogram of **u** = [110] MD lengths extracted from ECCI montages. Histogram bins were 10 μm (from 10 - 100 μm) and 100 μm (from 100 – 1300 μm) to better show the strong differences in MD length dispersions with normalization to the TDD of each process variant.

To study the effect of ALE purge time, Processes A (1 sec) and B (10 sec) are compared. The SiH_4 anneal pretreatment and TEGa-first ALE processes were held constant for both cases. Figure 2 provides representative ECCI micrographs of the resulting MD networks, taken with $\mathbf{g} = [\bar{2}20]$, clearly revealing that Process B (Fig. 2b) results in longer and fewer MDs than Process A (Fig. 2a). Figure 3a summarizes the average effective TDD (with standard error) for these two process variants. Process B exhibited a TDD of $(1.2 \pm 0.2)\times10^7$ cm^{-2}, 5× lower than that of Process A at $(6.8 \pm 1.0)\times10^7$ cm^{-2}. SFPs were also observed at a density of ~1×10^7 cm^{-2} in both variants.

To quantify the MD length differences between Processes A and B observed in Fig. 2, average MD length, $L_{MD}^{\langle 110\rangle}$, was determined according to Equation 2, the results of which are presented in Figure 3b for both line directions. The large error bar in the $\mathbf{u} = [\bar{1}10]$ Process B case is due to greater variance in TDD across the images sampled, indicating a wider dispersion in $L_{MD}^{[\bar{1}10]}$. Additionally, a more significant anisotropy in $L_{MD}^{\langle 110\rangle}$ (versus TDD) between the two line directions is visible, likely due to differences in α versus β dislocation glide velocities [4].

Figure 3c provides a histogram of directly measured $L_{MD}^{[110]}$ for Processes A and B; note that only $\mathbf{u} = [110]$ MDs, which were generally shorter than the orthogonal set, were measured in this manner. Here, it is clear that significantly longer MDs, and fewer short ones, are obtained via Process B. Taken together, this data indicates that increased dislocation glide lengths, and thus higher glide velocities, as well as decreased dislocation introduction rates, all result from the longer (10 sec vs. 1 sec) ALE purge time in Process B. These trends will be further analyzed in Section III.B.

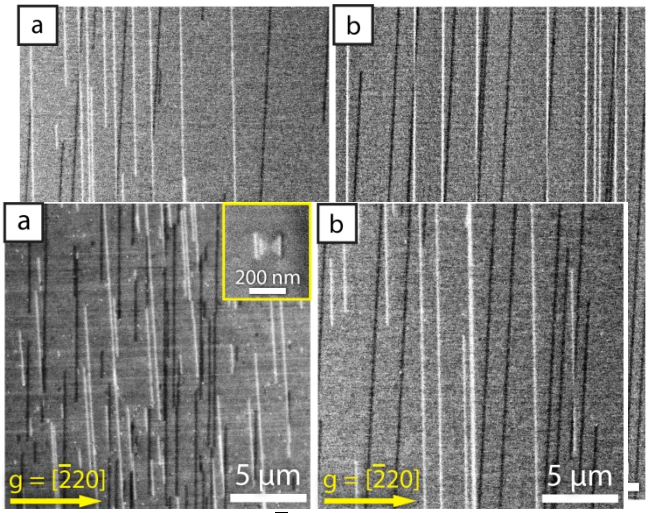

Figure 2: ECCI $\mathbf{g} = [\bar{2}20]$ micrographs comparing effect of ALE purge time on MD networks in (a) Process A, using 1 sec purges, and (b) Process B, using 10 sec purges.

2. *Impact of ALE-Initiation Precursor Species*

Next, the impact of the initial ALE precursor was studied by comparing Processes B (TEGa-first) and C (TBP-first), which both used the SiH_4 anneal pretreatment and 10 sec ALE purges. Figure 4 shows representative $\mathbf{g} = [\bar{2}20]$ ECCI micrographs of the

resulting MD networks. While many MD endpoints can be observed in Fig. 4a, most of the MDs in Fig. 4b extend completely through the 40 μm tall image, qualitatively suggesting longer MDs and a lower TDD. Note that where the bright and dark lines cross each other the resulting contrast cancellation creates a false appearance of endpoints; the lines are indeed continuous through these regions.

Figure 5a summarizes the TDD extracted from MD networks in both ⟨110⟩ directions, where a drastic reduction of ~10×, from (1.2 ± 0.2)×10^7 cm^{-2} to (1.1 ± 0.1)×10^6 cm^{-2}, is observed. The resultant difference in $L_{MD}^{\langle 110 \rangle}$ is also over an order of magnitude, as seen in Fig. 5b, with similar anisotropy between both line directions. Similarly, as seen in Fig. 5c, an equally clear difference in the $L_{MD}^{[1\bar{1}0]}$ distributions exists. In the case of Process C, ECCI montages over 1.2 mm long were needed to fully capture some of the longest MDs, and even then a few MDs still passed out of the total image area.

Because all other conditions were unchanged, we can conclude that the differences observed between Processes B and C are a direct result of switching the ALE initiation species from TEGa to TBP, respectively. As before, we can also conclude that this change results in improved dislocation glide behavior, yielding longer and fewer total dislocations for otherwise identical GaP/Si epilayers and growth processes.

ALE Initiation and GaP Thin-Film Stability

The outsized impact of merely changing the initiating precursor species (TEGa versus TBP) of the ALE nucleation process strongly suggests that some aspect of the resultant interfacial chemistry, or perhaps the nature of the ALE film itself, plays a critical role in MD evolution. ALE and related techniques are commonly employed to help enforce planar growth modes in heteroepitaxial cases where high interface energy, such as in GaP/Si [27], would otherwise result in Volmer-Weber growth. The low temperature and pulsed precursor delivery of ALE suppresses large-scale adatom diffusion and island formation, thereby promoting growth of a planar film [17], at least until the point where a bulk volume of sufficient stability to counteract the high interface energy has been produced. For GaP/Si, 5 – 25 ALE cycles (or approximately 1.4 – 6.8 nm) is typically found to yield adequate stability of the nascent GaP film [10], [12], [24]. It is also often observed that if an insufficient film volume (i.e. thermodynamic stability) has not been produced during the ALE process then subsequent temperature increases, with the attendant increase in atomic diffusivity and mass transport, results in island formation and film roughening [9], [12], [27].

The 15-cycle ALE process used for the work reported herein was originally developed based solely on the use of TEGa initiation, with the target of maintaining the ALE layer stability (surface morphology) during the ramp up to the bulk GaP growth temperature. However, a similar optimization investigation had not been performed for TBP. Therefore, to examine whether there is some inherent difference in the interfacial energetics or stability in the initial ALE GaP itself depending on the initiating precursor species, a few additional 100 nm GaP/Si samples were produced based on thinner TEGa- and TBP-initiated ALE nucleation layers (i.e. 5 cycles instead of 15). All other growth conditions were kept identical to Process A and C, respectively. The expectation here was that the lower inherent stability of the thinner ALE nucleation layer would amplify any critical differences between the two processes, resulting in observable differences once growth out to the 100 nm film thickness.

Figure 6 presents AFM micrographs of two representative samples from this experiment, wherein a clear difference in the terminal GaP surface morphology can be seen. R_q values of 2.46 nm and 0.98 nm were obtained for TEGa- (Fig. 6a) and TBP-initiated (Fig. 6b) cases, respectively. In the former, numerous pits and faceted features are observed, yielding nearly 3× higher

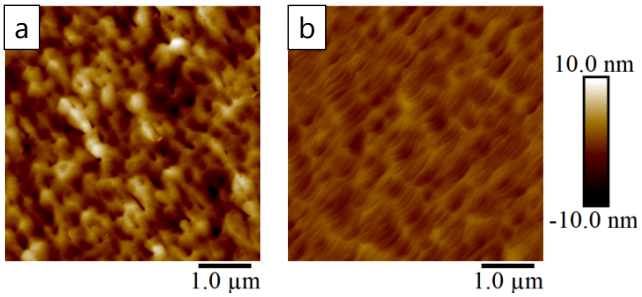

Figure 6: AFM micrographs of 100 nm GaP/Si epilayers grown using a 5-cycle ALE nucleation layer following (a) TEGa- and (b) TBP-initiated processes.

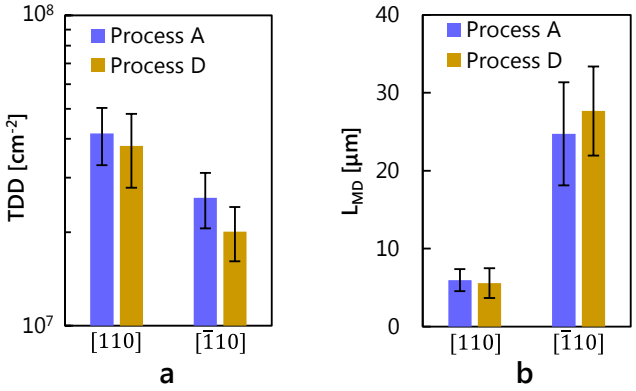

Figure 7: Examination of Si surface preparation effects via comparison of Processes A versus D in terms of (a) TDD and (b) average MD length for each MD line direction.

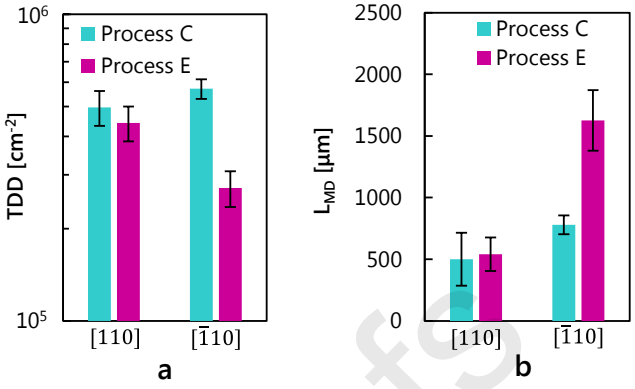

Figure 9: Examination of Si surface preparation effects via comparison of Processes C versus E in terms of (a) TDD and (b) average MD length for each MD line direction.

roughness than the R_q = 0.90 nm found for equivalent samples employing thicker (15-cycle) ALE nucleation layers. In contrast, the TBP-initiated samples exhibit a smooth, step-flow morphology and little faceting, with both appearance and roughness identical to the 15-cycle versions.

These results strongly suggest that the TBP-initiated ALE nucleation layers, and/or the resultant GaP/Si interface itself, are more stable (or at least more metastable) than the otherwise nominally identical TEGa-initiated layers, requiring a smaller volume of GaP material to balance the film-interface energetics [27]. Such a large influence of a relatively subtle process change is entirely consistent with the high sensitivity of the III-V/Si heteroepitaxial system toward substrate surface cleanliness and interfacial quality and its tendency toward nucleation related defect formation [18]. Potential mechanisms behind the improved stability (i.e. lower interfacial energy) of the TBP-initiated layers is discussed in Section IV.

3. Impact of Si Surface Pretreatment

To investigate the impact of the Si pretreatment processes on MD evolution and resultant TDD, two different comparison sets were considered: Processes A (SiH_4 anneal) versus D (Si_2H_6 epitaxy), making use of TEGa-first initiation and 1 sec purges, and Processes C (SiH_4 anneal) versus E (Si_2H_6 epitaxy), making use of TBP-first initiation and 10 sec purges.

Examining the former (A vs. D) set first, the MD networks seen via ECCI for Process D are indistinguishable from those of Process A (Fig 2a.) and are thus not shown here. This similarity can also be seen quantitatively in Figure 7, which reveals a lack of statistically significant variation in both TDD and $L_{MD}^{\langle 110 \rangle}$ for the two sample sets. Total TDD in both cases was relatively high at (6-7)×10^7 cm^{-2}, with average MD lengths in $\mathbf{u} = [110]$ and $[\bar{1}10]$ of ~5 µm and ~25 µm, respectively. Because these variants made mutual use of ALE process parameters (TEGa-first initiation, 1 sec purge) that were shown in the preceding sections to have a detrimental impact (higher TDD), it is possible that any effects related to the Si pretreatment process are simply being overshadowed.

As such, Processes C (SiH_4 anneal) and E (Si_2H_6 epitaxy), which used the lower-TDD ALE parameters, provide a better comparison. As shown by the $\mathbf{g} = [220]$ ECCI images in Figure 8, the $\mathbf{u} = [\bar{1}10]$ MD arrays of the two variants are very similar, with MD lines extending well beyond the frame of both cropped micrographs. However, a notably higher number of MD endpoints can be readily identified for Process C (Fig. 8a) than for E (Fig. 8b), suggesting shorter $L_{MD}^{[\bar{1}10]}$ for the former; the $\mathbf{u} = [110]$ MD arrays were effectively identical.

As presented in Figure 9, there is indeed a statistically relevant difference in $\mathbf{u} = [\bar{1}10]$ resolved TDD of ~2×, with attendant ~2× difference in $L_{MD}^{[\bar{1}10]}$, between Processes C and E, yielding total TDD values of 1.1×10^6 cm^{-2} and 0.7×10^6 cm^{-2}, respectively. While certainly non-negligible, this relatively small difference indicates that the Si pretreatment plays a diminutive role in determining TDD compared to the ALE-associated process variables. Nonetheless, the SiH_4 anneal process (A, C) was found to provide a slightly smoother GaP surface morphology, with R_q = ~0.8 nm versus the >1.0 nm of the Si_2H_6 epitaxy (D, E). Depending on specific needs and how this impacts subsequent epitaxy, Process C could be slightly favorable over E, despite the TDD differences.

B. Dislocation Introduction and Glide Dynamics

Although the achievement of very low TDD III-V/Si heterostructures is the overarching goal, understanding the underlying dislocation evolution — the fundamental introduction and glide dynamics — that ultimately leads to the observed TDD trends is crucial for the sake of informed optimization, portability, and scalability. Thus, we further analyze the results presented in the preceding sections to elucidate how the dislocation introduction and glide dynamics are impacted by the different process variables investigated.

1. Epilayer Plastic Strain Relief

To compare the dislocation dynamics across the sample variants, it is necessary to examine the relative relaxation state for the associated samples. The degree of epitaxial relaxation, or strain relief, can be resolved (and measured) in the two interface-parallel ⟨110⟩ directions, as determined by the total MD Burgers content in said directions. The strain-reliving Burgers vector component, $\boldsymbol{b}_{eff}$, of a 60° MD has a magnitude of $b/2$ and points orthogonal to the MD line direction. The average plastic strain relief in a specific direction, $\delta_{MD}^{\langle 110\rangle}$, is then given by:

$$\delta_{MD}^{\langle 110\rangle} = \rho_{MD}^{\langle \bar{1}10\rangle} \cdot b_{eff}^{\langle 110\rangle}, \tag{3}$$

where $\rho_{MD}^{\langle \bar{1}10\rangle}$ is the average linear density of MDs with line direction orthogonal to the strain relaxation [47]. Note that while generic indices are used in Eq. 3, the associated numeric values are resolved along specific $[110]$ direction directions; $[110]$ strain relief is provided by MDs with $\mathbf{u} = [\bar{1}10]$, whereas $[\bar{1}10]$ strain relief is provided by $\mathbf{u} = [110]$ MDs.

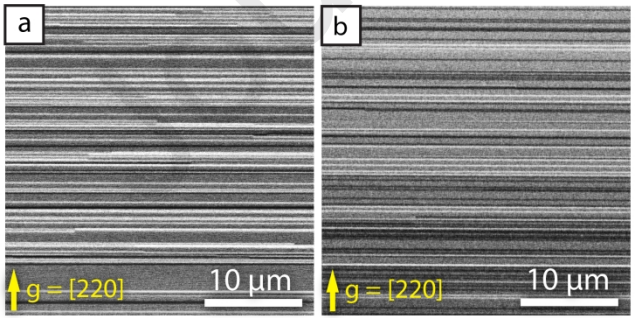

Figure 8: ECCI micrographs using $\mathbf{g} = [220]$ comparing effect of Si pretreatment conditions on MD networks in a) Process C, using the SiH_4 anneal, and b) Process E, using the Si_2H_6 buffer.

For the sake of comparison, average plastic strain relief may also be determined via in-plane lattice constants extracted from conventional room-temperature XRD RSMs. This average geometric plastic strain relief in a specific ⟨110⟩ direction via XRD, $\delta_{XRD}^{\langle 110\rangle}$, is given by:

$$\delta_{XRD}^{\langle 110 \rangle} = f - \frac{a_{\parallel} - a_r}{a_r}, \quad (4)$$

where f is the lattice mismatch at room temperature, $a_{\parallel}$ is the in-plane lattice constant of the strained GaP epilayer, and a_r is the relaxed lattice constant of GaP. Given the thinness and mostly-strained nature of these films, some inaccuracies in $\delta_{XRD}^{\langle 110 \rangle}$ measurements are expected, as well as spatial inhomogeneity, and thus it is interesting to compare $\delta_{XRD}^{\langle 110 \rangle}$ against $\delta_{MD}^{\langle 110 \rangle}$, a more direct measurement of plastic strain relief based on sampling the responsible MD populations. Table 2 lists the ECCI-based $\delta_{MD}^{\langle 110 \rangle}$ and XRD-based $\delta_{XRD}^{\langle 110 \rangle}$ measurements for all process variants examined in this work.

Table 2: Average plastic strain relief at room temperature for each process variant via MD line density and XRD measurements. A general 7×10^{-5} error in XRD strain values is estimated due to the epilayer thinness and asymmetric strain state of these 100 nm films.

Process	$\delta_{MD}^{[\bar{1}10]}$ [$\times10^{-4}$]	$\delta_{XRD}^{[\bar{1}10]}$ [$\times10^{-4}$]	$\delta_{MD}^{[110]}$ [$\times10^{-4}$]	$\delta_{XRD}^{[110]}$ [$\times10^{-4}$]
A	2.29 ± 0.25	1.65	5.29 ± 0.42	4.77
B	1.76 ± 0.69	1.65	4.64 ± 0.53	3.30
C	2.39 ± 0.98	1.83	4.28 ± 0.28	3.49
D	2.03 ± 0.43	1.83	5.34 ± 0.30	3.30
E	2.30 ± 0.50	2.11	4.24 ± 0.30	3.67

With the exception of the $\delta^{[110]}$ results for Processes A and D, the process variants do not differ substantially from each other in terms of average plastic strain relief. For the most part, $\delta_{XRD}^{[\bar{1}10]}$ is found to reside within the estimated uncertainty of the associated $\delta_{MD}^{[\bar{1}10]}$ value (as determined via error propagation from the measured $\rho_{MD}^{[110]}$), and by no more than 6.4×10^{-5} in the worst case. As this is roughly equal to the expected error in the XRD measurements on these thin films, we can consider the two sets of values to be in reasonably good agreement. At least some of the small systematic discrepancy that does exist can be attributed to the use of the typical tetragonal distortion approximation for calculating relaxation from the XRD measurements, even though it is not completely valid here [48]. The slightly larger discrepancy between $\delta_{MD}^{[\bar{1}10]}$ and $\delta_{XRD}^{[\bar{1}10]}$ may be receiving additional contributions from the offcut induced tilting present in this direction [48], [49].

Effectively equal final plastic strain relief (relative to total misfit, f, which is 3.6×10^{-3} at 300K) and thus total MD length per given area [5], is found across all samples. However, given the wide range of TDD measured across the same samples, this result indicates that that the dislocation introduction and glide dynamics must vary significantly between the process sets. Based on conventional mismatched epitaxy theory, and assuming all else being equal, for these samples to all yield the same final relaxation state it must follow that the process variants exhibiting high TDD suffer from comparatively high dislocation introduction rates brought on by low glide velocities, while low TDD indicates low introduction rates and high glide velocities [6], [50]. The following sections serve to quantify these trends.

2. Dislocation Introduction Dynamics

Given the nominally identical growth rates, temperatures, and epilayer thicknesses of the different sample sets investigated, the total TDD values (see Table 1), which span two orders of magnitude, provide an indication of the relative dislocation introduction rates and the associated impact, at least indirectly, of the investigated process variables. However, this after-the-fact view is blind to the dynamic and typically non-linear nature of dislocation introduction during lattice-mismatched epitaxy [6], [7], [51], [52], and thus provides little new insight.

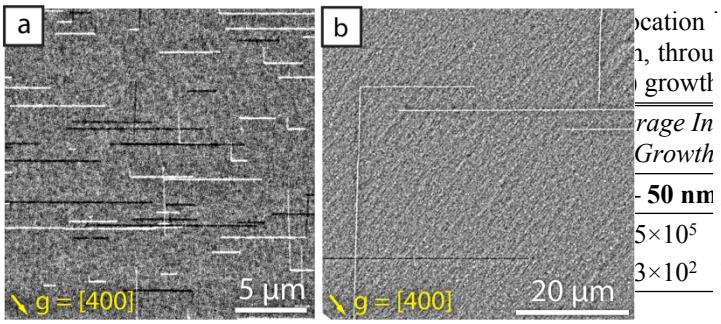

Figure 10: **g** = [400] ECCI micrographs revealing MDs with both ⟨110⟩ line directions in 50 nm samples from (a) Process A (TEGa-first / 1 sec purge) and (b) Process C (TBP-first / 10 sec purge).

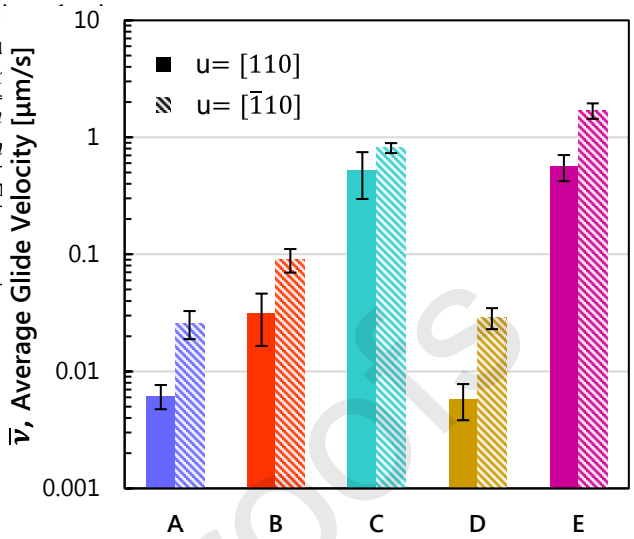

Figure 11: Calculated average MD glide velocity, *v*, for all process variants, resolved for both **u** = [110] and [$\bar{1}$ 10] line directions.

Therefore, to supply additional detail to this analysis a few samples of Process variants A and C were grown to a total thickness of only 50 nm, or half that of the 100 nm thick layers discussed up to this point, thereby enabling a probe of the initial introduction behavior just beyond critical thickness. As presented in Figure 10, ECCI (using **g** = [400] for visibility of MDs with both ⟨110⟩ line directions) shows the very early stages of MD network formation, from which total TDD of 2.5×10^{7} cm^{-2} for Process A and 7×10^{4} cm^{-2} for Process C is estimated. Thus, a more than two order of magnitude discrepancy in dislocation introduction rate for the high-TDD (TEGa-first / 1-sec purge) versus low-TDD (TBP-first / 10-sec purge) process set is resident from the very onset of relaxation. Total plastic strain relief (δ_{MD}^{total}) extracted from ECCI micrographs of these 50 nm samples was found to be 4.4×10^{-5} and 2.8×10^{-6} for Process A and C, respectively. These small plastic strains, which are well within the error of XRD measurement, are effectively negligeable relative to the plastic strains at 100 nm (see Table 2).

In addition to the starkly different absolute numbers, comparing the total TDD at the 50 nm and 100 nm thicknesses for these two variants also reveals distinctly different dynamical behaviors. For the low- TDD Process C, just over 6% of the dislocation population at the final 100 nm thickness is present by the 50 nm point, suggesting either a relatively monotonic introduction rate that only begins at around the critical thickness or a more non-linear trend skewed toward higher layer thicknesses. Conversely, for the high-TDD Process A, 37% of the terminal TDD is already present at the same thickness, indicating a comparatively front-loaded introduction rate trend.

Assuming that dislocation introduction does indeed begins at approximately 40 nm, as we have previously observed [28], the average rates of introduction within early (40 – 50 nm) and late (50 – 100 nm) stages of GaP heteroepitaxial growth for Processes A and C can be estimated and are given in Table 3. Between these two variants the introduction rate differs by nearly 350× at the onset of relaxation in the early stage and then reduces to just over 40× during the late stage. The narrowing difference is the result of the Process A introduction rate slowing by ~3× between the early and late stages, while the Process C rate accelerates by about the same amount. This late onset of dislocation introduction in Process C is consistent with observations on mismatched III-V thin films [52] and bulk materials [4] for which dislocation blocking may initially occur [53]. Although this data is too coarse to enable a more detailed trend analysis, these results do at least suggest a lower energetic barrier to dislocation nucleation, or perhaps the existence of some heterogenous nucleation source, in Process A as compared to Process C.

3. Dislocation Glide Dynamics

Table 4: Dislocation dynamics metrics calculated from direct-measured $\mathbf{u} = [110]$ MD lengths for Process A, B, and C. Where two values are given for $\acute{L}_{MD}^{[110]}$ and $\acute{v}$, the first represents the mean, while the value in parentheses is extracted from the maximum observed MD length.

Process	$\acute{L}_{MD}^{[110]}$ [µm]	$\acute{v}$ [µm/s]	$\acute{\delta}_{MD}^{[\bar{1}10]}$ [×10^{-4}]
A	8.1 (59)	0.008 (0.061)	1.88
B	22.9 (112)	0.024 (0.117)	1.56
C	264.5 (1240)	0.275 (1.292)	2.30

Given the similar relaxation, but different dislocation introduction rates and trends, it follows that dislocation glide velocities are varying in a similar manner. In general, the average glide velocity, v, for some given length of growth time, Δt, is given by

$$v = \frac{\Delta L_{MD}^{\langle 110 \rangle}}{2 * \Delta t}, \quad (5)$$

where $\Delta L_{MD}^{\langle 110 \rangle}$ is the resultant change in average MD length due to glide [50]. To a first degree, an ensemble average glide velocity may be estimated for the standard 100 nm thick GaP/Si samples using the full average MD length determined via Eq. 2, again taking the 40 nm film thickness as the onset of dislocation introduction. The results of this analysis, comparing all five process variants, are presented Figure 11. Of course, this analysis provides no insight into the instantaneous glide velocities that may be occurring for individual dislocations at any given time, but the ensemble averages, which are found to span orders of magnitude, do suggest that significant glide hindrances are occurring in Processes A and D (and to a lesser extent, B). The stepwise increase in v from Process A to B to C indicates that overall higher dislocation glide velocities (i.e. reduction in numbers and/or severity of glide hindrances) are achieved through the use of longer ALE purges (A → B) and with a TBP-first ALE process (B → C).

To extract additional quantitative detail regarding dislocation glide dynamics for these three process variants (A, B, and C), we can also extract average glide velocities using MD length data directly measured from long ECCI montages, like those presented in Figs. 3(c) and 5(c). For this analysis we note that only $\mathbf{u} = [110]$ MD length data is available due to practical constraints in producing sufficiently long image areas. Total montage lengths of >1 mm were required to capture some of the longest $\mathbf{u} = [110]$ MDs, whereas the ensemble average lengths for the $\mathbf{u} = [\bar{1}10]$ MDs, as discussed throughout Section III.A, were found to be at least 2× longer and denser for every process variant, making such measurements intractable. Because the general trends observed were similar in both directions, this analysis, despite the reduced dimensionality, is still expected to be relevant.

Table 4 presents the dislocation dynamics metrics extracted via the direct-measurement approach. To differentiate from values determined using the ensemble approach in the preceding sections, the direct-measurement values are indicated with the inclusion of an accent mark. First, direct-measured mean and max $\mathbf{u} = [110]$ MD lengths, $\acute{L}_{MD}^{[110]}$, are given. Average and upper $\acute{v}$ estimates are then calculated based on these vales (with respect to the 40 nm starting point), setting $\Delta L_{MD}^{[110]} = \acute{L}_{MD}^{[110]}$. By summing the total MD length, $\Sigma \acute{L}_{MD}^{[110]}$, normalized by the area sampled, the associated MD line density is recovered. Plastic strain relief at room temperature, $\acute{\delta}_{MD}^{[\bar{1}10]}$, is then calculated from this density using Eq. 3.

We find generally good consistency, if not perfect agreement, between these calculated plastic strain relief values (Table 4) and the associated results in Table 2, verifying the relative accuracy of ECCI- and XRD-based analysis methodologies. Similarly, these values also generally agree with those in Figure 11. The main exception is $\acute{v}$ for Process C, which is somewhat underestimated in the direct-measurement approach due to the difficulty in capturing the full length of some of the extremely long MDs. The upper $\acute{v}$ estimates based on the maximum $\acute{L}_{MD}^{[110]}$ values were typically at least 5× larger than the associated average for each variant, highlighting the wide dispersion of actual glide velocities experienced by individual dislocations. If we consider the longest individual MDs observed as representative of the most relatively unhindered glide dynamics within a given sample, a variation of only ~2× is found between Process A and B, whereas over an order of magnitude difference is observed for Process C; it is possible the difference is even greater given the aforementioned practical measurement limits. Nonetheless, these

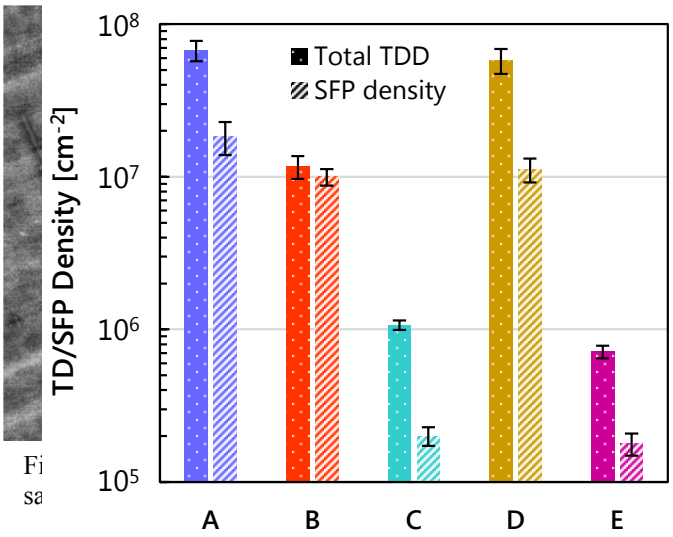

Figure 13: Average TDD and SFP densities observed for all process variants.

Table 5: Average glide velocity, v, over both MD line directions, through early (40 – 50 nm) and final (50 – 100 nm) growth stages.

	v [μm/s]	
Process	**40 – 50 nm**	**50 – 100 nm**
A	0.023 ± 0.004	0.012 ± 0.004
C	0.56 ± 0.28	0.69 ± 0.29

observations suggest only slightly fewer hindrances to glide in Process B versus A, while a more substantial change is responsible for the improvements in Process C.

Finally, similar to the introduction rate analysis presented in Table 3, the ensemble dislocation population measurements from the 50 nm and 100 nm thick Process A and C samples can be used to resolve average glide velocities for the early (40 – 50 nm) and late (50 – 100 nm) GaP epilayer growth stages; the results are presented in Table 5. For Process A, a 2× decrease in glide velocity between the early and late stages is observed, perhaps suggesting a slight increase in glide hindrances as more relaxation occurs. At 50 nm, the plastic strain is already ~10% of the level reached by 100 nm; this supports the observation of a slightly faster glide velocity in this early stage, after which the diminishing elastic strain may be leading to the decreased glide velocity. Process C, on the other hand, shows a small (~20%), potentially negligible (i.e. within error bounds) increase, suggesting that little is changing within the fundamental dislocation dynamics for this variant. For Process C, at 50 nm the plastic strain is only ~1% of the level at 100 nm, thus the stress to affect dislocation glide is likely steadier throughout. It should be noted that the traditional dislocation glide mechanics model with modest stress coupling [4] cannot describe the nearly 60× difference in glide velocity between Processes A and C; all else being equal, a ~15× higher stress would be required in Process C for this to be true. Given the similar final degree of plastic strain relief (and thus film stress) at 100 nm of these two variants, the glide velocity stress dependence cannot account for the substantial difference between Processes A and C [4].

Overall, dislocation introduction and glide trends were found to vary significantly among the process conditions, consistent with the TDD results discussed previously. The dislocation dynamics, both in terms of introduction rates and glide velocities, are also found to evolve differently throughout the growths for two of the process variants. For Process A there appears to be a relatively high dislocation introduction rate at the relaxation onset, with relatively slow glide thereafter. Conversely, Process C exhibits low initial introduction and much faster glide. Given the somewhat negligible effect of the Si pretreatment, Process D and E likely follow similar trends as A and C, respectively. Process B appears to sit in between the two, although closer to Process A than C. Ultimately, all the process variants reach the same effective overall relaxation, but through very different paths.

C. Stacking Fault Pyramids

Finally, we consider the occurrence of stacking fault pyramids (SFPs) and their potential correlation with the TDD and underlying dislocation dynamics. As seen in Figure 12, which presents a representative ECCI micrograph of a Process A sample, a significant number of SFPs are visible. Some fraction of them are found to lie in intersection with MDs, appearing to serve as either termination or introduction points. Similar observations were previously

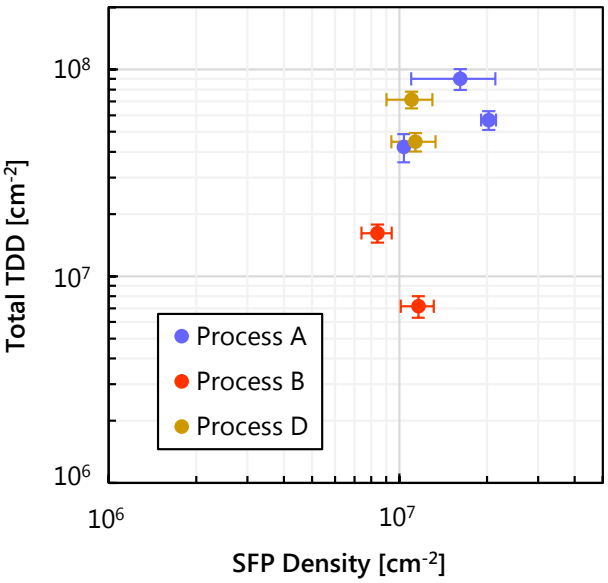

Figure 14: Correlation plot of SFP density and TDD across individual TEGa-first GaP/Si samples.

reported by Feifel et al. [24], who concluded that SFP-MD interactions were likely serving as critical dislocation glide hindrances, and thus ultimately played a key role in the generation of excess TDD.

Figure 13 summarizes the populations of SFPs and total TDD measured for all process variants examined herein. The average SFP density is generally found to be around 3–5× lower than the TDD for any given variant, with the exception of Process B where they are nearly equal. The TEGa-initiated variants (A, B, and D) all exhibit average SFP densities of $\geq 10^7$ cm^{-2}, whereas the TBP-initiated variants (C and E) both possess SFP densities of $\leq 2\times10^5$ cm^{-2}. As such, the SFP densities indeed trend similarly to TDD, which does suggest some degree of correlation.

Nonetheless, taking the case of Process A (Fig. 12) as an example, possessing the highest SFP population overall, we find that only ~5% of the MDs appear to be terminated by a stacking fault, and only ~10% of the MDs are even relatively proximal (i.e. within ~100 nm) to SFPs. Such a low rate of SFP-MD coincidence seems unlikely to be able to account for the orders of magnitude higher dislocation introduction rates in the TEGa-initiated variants versus the TBP-initiated cases. That is, even if the SFPs completely block the glide of any MDs that ultimately run into them, the remaining ~95% of the MDs remain unblocked. However, from the MD length analyses presented in the preceding sections (e.g. Figs. 3 and 5), the problem of slow glide velocities in the TEGa-initiated variants is effectively spread across the entire MD population rather than just a small fraction.

In the case of Process B, a similar coincidence of SFPs with MDs is observed. However, a TDD reduction of 5× compared to Process A is observed, whereas the reduction in SFP density is <2×. Given that Process B shows a >5× reduction in TDD and >3× higher glide velocity at about the same SFP density as the other TEGa-initiated variants, it seems unlikely that dislocation glide has any strong correlation with the presence of SFPs. The low fraction of MDs in proximity to SFPs suggests a secondary, rather than primary effect of SFPs on TDD and glide velocity.

To examine whether any trends relating SFP density to TDD may be getting lost due to averaging over multiple samples within a given variant (as in Fig. 13), Figure 14 displays the SFP and MD endpoint populations of individual samples from Processes A, B, and D, where detailed SFP characterization was performed. Here, the samples all exhibit SFP densities clustered around (1-3)$\times10^7$ cm^{-2}, but possess TDD that vary by over an order of magnitude, from 7×10^6 cm^{-2} to 9×10^7 cm^{-2}. This correlation is considerably weaker than the effect of the other process variables on TDD. That said, a simple Pearson correlation analysis yields a coefficient of $r = 0.5$, suggesting that there is indeed some correlation between the two defect populations. Nonetheless, this result does not rule out other causes, for which high SFP density and TDD both may be associated effects. As such, while the observed SFP-MD interactions may indeed be leading to a degree of glide hinderance for the MDs involved, we can still conclude that the SFPs are not the primary contributor to excess dislocation introduction.

That said, the clustering of Processes A and D, versus Process B as the outlier, suggests that neither the Si pretreatment method nor the ALE purge time has a strong impact on SFP populations. The drastic reduction in SFP densities found for Processes C and E indicates that it is the ALE initiation species, TBP versus TEGa, that matters most. Additionally, given that the TDD trends almost identically as the SFP density, it is likely that the high SFP

densities, high early stage dislocation introduction rates, and hindered glide in the TEGa-initiated variants (A, B, and D), as opposed to the TBP sets (C and E), are strongly interrelated and possibly driven by the same underlying mechanism.

IV. DISCUSSION

Having observed the direct results (TDD, MD length, film stability, etc.) of the process conditions, as well as linking those to indirect observations of dislocation dynamics and SFP populations, we now discuss the linkages between these observations and the process conditions. First, we tie the TDD trends all the way to the growth process variables. Lastly, missing links of epitaxial processes occurring at the interface and the chemistry and structure of the interface are proposed to further tie in the observed SFP populations and dislocation dynamics.

D. Process Conditions versus TDD Trends

The average total TDD measured for each of the process variants is provided in Table 1, and we discuss the trends observed here. Overall, a 63× reduction in TDD is achieved by switching from the original TEGa-first / 1 sec purge conditions to the TBP-first / 10 s purge set (A → B → C). Given the available data, the majority of this reduction (~11×) is attributed to the initial ALE precursor choice, which thus suggests some kind of dependence on the interfacial chemistry; this topic is discussed further in Section IV.B.

The remaining (~6×) reduction is attributed to the longer ALE purge time. Because comparable samples using TBP-first initiation and short (1 s) purges were not examined in this effort, it is not possible to fully deconvolute the balance in benefit between the initiation precursor and purge time. As such, while the purge time appears to have a slightly smaller impact, it is still clearly significant. Given that the ALE nucleation layer growth ends well below the critical thickness for dislocation introduction and/or glide, the fact that TDD reduction is nonetheless observed indicates some kind of impact on the GaP material itself, or the growth thereof.

Considering the pumping speed and total volume of the MOCVD reactor used in this work, a full purge requires at least 8 sec. As such, 1 sec cycles likely results in TBP and TEGa gas-phase mixing, with the potential for deleterious reactions and clustering occurring on the substrate surface or potentially the gas phase just prior to the surface. Additionally, previous spectroscopic observation of GaP/Si growth via pulsed chemical beam epitaxy (similar conditions to ALE) suggested relatively slow surface incorporation kinetics for Ga and P from TEGa and TBP precursors [18], especially for surfaces under continual TBP exposure [54]. Thus, the longer 10 sec purges not only support the single-species, layer-by-layer growth mode that is intended within the ALE process by fully clearing each precursor from the reactor, but the additional time provided for surface reactions and adatom diffusion likely also yields higher GaP epitaxial film quality and thus more favorable MD evolution [43].

In the high-TDD cases (A and D) the Si pretreatment appears to have little to no impact. However, once the two stronger factors governing TDD are addressed (i.e. ALE initiation precursor and purge time), use of the Si_2H_6 epitaxy is found to provide a slight improvement in TDD versus the SiH_4 anneal. This small difference may stem from a more effective burial of surface contaminants, like carbon, afforded by the Si homoepitaxy during the Si_2H_6 pretreatment. This effect would be consistent with that observed in our previous MBE-based GaP/Si investigations [10].

As mentioned, several other process parameters, including ALE precursor flow rate, ALE substrate temperature, and reactor pressure, were also screened, but were not found to significantly impact the resultant defect populations. That said, these studies were somewhat limited in scope and were performed using the TEGa-first initiation and 1 sec purge ALE process parameters, which are now recognized as detrimental. As such, similar to the Si pretreatment case, these variables could have small trends that were effectively masked, and further work to vary other process conditions under TBP-initiated, long-purge ALE conditions may enable further TDD reduction.

E. Interfacial Epitaxial Processes and Chemistry

The observed changes in TDD, SFP population, and film stability resulting from the choice of initial ALE precursor all suggest that some fundamental change of growth mechanism and/or chemistry at the GaP/Si interface is the primary controlling factor. Early work on MBE growth of GaP/Si demonstrated that exposing the Si to P prior to MEE could improve the self-annihilation of antiphase domains (in which antiphase boundaries are tilted, non-{110}-type [55]) and the prevention of 3D growth [56]. In MOCVD, ALE initiation with TBP (*tert*-butylphosphine) has been shown to help with the elimination of planar SFs [12]. While the geometry of SFPs suggests they are directly formed from defects at the GaP/Si interface, and thus exist since effectively the beginning of the growth [42], [43], dislocations do not reach the interface until well after, and thus must only be indirectly (even if strongly) affected by the specific interfacial structure and/or chemistry.

To examine what sort of fundamental changes at the interface could lead to such significant microstructural differences, we first consider the polarity of the GaP grown on Si to help determine the predominant interfacial bonding configuration. Asymmetric dislocation decoration etching conducted on our samples (see Supplemental info) [57], in combination with cross-sectional scanning transmission electron microscopy (STEM) imaging [13], suggests that the GaP in both TEGa- and TBP-initiated cases possesses an effective (111)A offcut (i.e. toward the [110]). Therefore, in both cases, the GaP film is Ga-polar (i.e. Ga at the top of the Ga-P "dumbbells" when viewed down the $[\bar{1}10]$ direction) [55]. Conversely, while convergent beam electron diffraction (CBED) analysis by Beyer et al. also indicated polarity invariance when switching between TBP- and TEGa-initiated ALE [55], they report that all of their samples were actually P-polar (i.e. P at the top of the Ga-P dumbbells when viewed down $[\bar{1}10]$).

The opposite reported polarities are likely the result of Si surfaces with different dimer reconstruction orientations. For the P-polar structures [12], [55], the use of exact (001)-oriented Si substrates and the specialized annealing processes in an atmospheric pressure (high H_2 partial pressure) MOCVD reactor resulted in the formation of thermodynamically-unfavorable D_A-type (i.e. Si surface dimers oriented perpendicular to the step edges) double height steps. However, for the Ga-polar samples presented herein, the combination of Si substrate vicinality and use of a low-pressure (low H_2 partial pressure) reactor is expected to yield a prevalence of thermodynamically-favored D_B-type steps (i.e. Si surface dimers oriented parallel to the step edges) [58]–[60]. The heteroepitaxial GaP grown on these two starting surfaces should indeed differ by an effective 90° rotation about the [001] axis, and thus opposite polarities as viewed down the $[\bar{1}10]$ zone.

Nonetheless, regardless of the specific polarity, which itself is more of a relative descriptor, when taking into account the Si dimer direction and GaP polarity, and assuming an abrupt interface, Ga–Si bonding across the heterovalent interface is expected and/or observed in all cases [55]. In fact, observation of P–Si bonding has only been reported when the initial TBP pulse was conducted at 675°C, far above the <500°C used in most ALE nucleation processes [55]. The uniqueness of that particular result suggests that either relatively high temperatures or the presence of TEGa is ultimately necessary to sufficiently decompose the TBP to allow for stable P deposition as the first monolayer.

On its face, this conclusion appears to contradict the clear differences observed for TEGa versus TBP initiation presented up to this point. However, given the apparent aforementioned lack of first-layer P deposition via TBP-initiation at typical ALE conditions (~450°C), a passivating effect of TBP on the Si surface is proposed. Recent STEM imaging by Beyer et al. has revealed an amorphous layer resulting from the very first TBP-initiated ALE cycle, suggesting that non-pyrolyzed TBP and/or TBP fragments are adsorbed onto the Si surface [61]. This mechanism is consistent with both *in situ* optical characterization experiments [16], [18], theoretical predictions [62], and a wealth of studies on organic functionalization of Si surfaces [63], [64].

A similar organic coating stemming from TEGa exposure onto Si surfaces has also been reported by Werner et al. [65]. However, they also revealed that Ga deposition, via both TMGa and TEGa, also results in the formation of

Ga-Si alloyed surface mounds and local substrate melt-back. Although this effect was shown for Ga doses of 1.5 monolayers, it is likely that coverages closer to even single monolayers, like those used for the growths presented herein, will also produce similar structures (albeit smaller and more sparsely distributed). Given that the SFPs observed in our samples appear to originate at the GaP/Si interface, and that SFPs are indeed generally believed to form at surface defects [42], such TEGa-induced non-planar surface structures are obvious candidates for their source. As such, the two orders of magnitude reduction in SFP density observed for the TBP-initiated process variants versus the TEGa-initiated cases is also consistent with a TBP-induced passivation mechanism that effectively limits the amount of Ga that is able to reach the Si surface, promoting stoichiometric GaP crystal growth instead of Ga-Si alloying driven by excess Ga accumulation.

Structural changes to the interface may also be occurring, depending on the initial precursor, resulting in different degrees of abruptness (e.g. to minimize the net dipole) and/or differing interfacial energies. Such compensated interfaces are shown by DFT modeling to be considerably lower energy than abrupt interfaces with exclusively P–Si or Ga–Si bonds [25], [66]. Detailed STEM characterization of GaP/Si interfaces has revealed the existence of a nanofaceted structure with a theoretically lower interfacial energy [26]. In that study, accompanying simulations suggested that kinetic factors, including the reduced diffusivity of P adatoms, contribute to the formation of the observed nanofaceted structures, rather than random interdiffusion processes. A more recent cross-sectional STM investigation of GaP/Si has also found similar interface structures possessing regions with abrupt (001) character and regions with non-abrupt character displaced by 4 to 6 monolayers from the base Si surface [67]. Samples in both of these studies were grown using similar conditions to those of Processes C and E in this present work: TBP-initiated ALE at 450°C on 2° offcut Si(001).

The impact of the initiating precursor on TDD seems to be less straightforward. Given the higher degree of film stability results for 5-cycle ALE films (Section III.A.2), it appears that using TBP-initiation yields either reduced interfacial energy or reduced bulk film energy, or some combination of the two. The former is plausible given the observations of interface restructuring and the TBP passivation effect previously discussed. The latter, possibly a consequence of higher quality growth (e.g. fewer point defects), is difficult to verify, but the proposed "templating" effect of TBP for reducing adverse Ga-related defects is a plausible mechanism. Both effects could be linked to TDD. The former would alter the energetic landscape near the interface, thereby impacting dislocation nucleation barriers [49] and glide activation energies or barriers [53]. In the latter case, point defects and other inhomogeneities would cause drag on gliding dislocations [4], [68] and give rise to heterogeneous nucleation sources [6].

It is likely that the effect of longer precursor purges (Process B vs. A or D) serves to reduce some of these inhomogeneities stemming from the TEGa-first process by either avoiding gas phase interactions or providing more time for adatom diffusion, or both, resulting in increased crystalline quality. This results in a >3× higher glide velocity and >5× reduction in TDD, with a relatively unchanged population of SFPs. Here, increased crystalline quality could explain the slightly more favorable glide and nucleation dynamics from Process A to B. However, without TBP passivation to mitigate SFP formation their populations remain unchanged.

The further ~10× TDD reduction from Process B to C, as well as the SFP reduction, seems to stem from the lower energy interface, TBP passivation effect, and potentially further improvements to crystalline quality. That said, it is plausible that the longer ALE purges, which affect growth after the initial layer, have the greater effect on crystalline quality. Thus, both interfacial energy reduction (primarily stemming from the initial ALE species) and crystalline material quality improvements (primarily stemming from the longer ALE purge times) have a profound impact on dislocation dynamics and the resultant TDD. While SFPs correlate with TDD, it is more likely that the underlying interfacial energy reduction — and to a lesser degree, crystalline quality improvement — is the mechanism behind more favorable dislocation evolution. Further study of these direct links is still needed.

V. SUMMARY

The exhaustive studies presented herein elucidate a number of important correlations between GaP/Si nucleation process conditions and TDD via intermediate factors of dislocation dynamics, SFP populations, and interface chemistry. Si pretreatment conditions are found to have only a slight effect on MD evolution and SFPs when not masked by other effects. Increasing the ALE purge time results in >5× TDD reduction, via increased dislocation glide, with little effect on SFP populations. The choice of initial ALE precursor was found to be the most sensitive variable: TBP-initiated ALE results in over an order of magnitude reduction in TDD and SFP populations achieved via increased dislocation glide velocity and decreased dislocation introduction. Additionally, thinner TBP-initiated ALE was found to have greater stability. Across all TEGa-initiated samples, SFP populations do not show strong correlations with TDD, nor do MDs interact significantly with SFPs. Thus, SFPs have a secondary effect on MD evolution. Rather, the interfacial structure and chemistry affected by the initial ALE species appear to be the primary cause of the observed film stability, SFP populations and MD evolution. An improvement in crystal quality stemming from the longer ALE purges can account for some degree of increased dislocation glide and reduced dislocation introduction as a secondary effect.

This work ultimately highlights that the heterovalent GaP/Si interface itself can be the source of very non-ideal defect evolution and thus become the sole limiter of further low-TDD III-V/Si development. By making use of the large-format defect imaging capabilities of ECCI as feedback to MOCVD process conditions, process conditions are uncovered that lead to substantially improved MD evolution with TDD $<1\times10^{6}$ cm^{-2}. Both the low-TDD combined with the enhanced understanding of the GaP/Si interface are critical to further development and scaling of low-TDD III-V materials integrated on Si.

REFERENCES

[1] M. Yamaguchi and C. Amano, “Efficiency calculations of thin-film GaAs solar cells on Si substrates,” *J. Appl. Phys.*, vol. 58, no. 9, pp. 3601–3606, 1985, doi: 10.1063/1.335737.

[2] C. L. Andre, J. J. Boeckl, D. M. Wilt, A. J. Pitera, M. L. Lee, E. A. Fitzgerald, B. M. Keyes, and S. A. Ringel, “Impact of dislocations on minority carrier electron and hole lifetimes in GaAs grown on metamorphic SiGe substrates,” *Appl. Phys. Lett.*, vol. 84, no. 18, pp. 3447–3449, 2004, doi: 10.1063/1.1736318.

[3] D. Jung, R. Herrick, J. Norman, K. Turnlund, C. Jan, K. Feng, A. C. Gossard, and J. E. Bowers, “Impact of threading dislocation density on the lifetime of InAs quantum dot lasers on Si,” *Appl. Phys. Lett.*, vol. 112, no. 15, 2018, doi: 10.1063/1.5026147.

[4] I. Yonenaga, “Mechanical properties and dislocation dynamics in III-V compounds,” *J. Phys. III*, vol. 7, no. 7, pp. 1435–1450, Jul. 1997, doi: 10.1051/jp3:1997198.

[5] M. S. Abrahams, L. R. Weisberg, C. J. Buiocchi, and J. Blanc, “Dislocation morphology in graded heterojunctions: GaAs1-xPx,” *J. Mater. Sci.*, vol. 4, no. 3, pp. 223–235, 1969, doi: 10.1007/BF00549922.

[6] R. Beanland, “Multiplication of misfit dislocations in epitaxial layers,” *J. Appl. Phys.*, vol. 72, no. 9, pp. 4031–4035, Nov. 1992, doi: 10.1063/1.352257.

[7] A. Y. Kim, “Evolution of microstructure and dislocation dynamics in InxGa1-xP graded buffers grown on GaP by metalorganic vapor phase epitaxy: Engineering device-quality substrate materials,” *J. Vac. Sci. Technol. B Microelectron. Nanom. Struct.*, vol. 17, no. 4, pp. 1485–1501, 1999, doi: 10.1116/1.590779.

[8] H. B. Pogge, B. M. Kemlage, and R. W. Broadie, “The heteroepitaxial growth of GaP films on Si substrates,” *J. Cryst. Growth*, vol. 37, no. 1, pp. 13–22, 1977, doi: 10.1016/0022-0248(77)90138-5.

[9] Y. Takagi, H. Yonezu, K. Samonji, T. Tsuji, and N. Ohshima, “Generation and suppression process of

crystalline defects in GaP layers grown on misoriented Si(100) substrates," *J. Cryst. Growth*, vol. 187, no. 1, pp. 42–50, 1998, doi: 10.1016/S0022-0248(97)00862-2.

[10] T. J. Grassman, M. R. Brenner, S. Rajagopalan, R. Unocic, R. Dehoff, M. Mills, H. Fraser, and S. A. Ringel, "Control and elimination of nucleation-related defects in GaP/Si(001) heteroepitaxy," *Appl. Phys. Lett.*, vol. 94, no. 23, pp. 1–3, 2009, doi: 10.1063/1.3154548.

[11] S. L. Wright, M. Inada, and H. Kroemer, "Polar-on-nonpolar epitaxy: Sublattice ordering in the nucleation and growth of GaP on Si(211) surfaces," *J. Vac. Sci. Technol.*, vol. 21, no. 2, pp. 534–539, Jul. 1982, doi: 10.1116/1.571755.

[12] K. Volz, A. Beyer, W. Witte, J. Ohlmann, I. Nmeth, B. Kunert, and W. Stolz, "GaP-nucleation on exact Si (0 0 1) substrates for III/V device integration," *J. Cryst. Growth*, vol. 315, no. 1, pp. 37–47, 2011, doi: 10.1016/j.jcrysgro.2010.10.036.

[13] T. J. Grassman, J. A. Carlin, B. Galiana, L. M. Yang, F. Yang, M. J. Mills, and S. A. Ringel, "Nucleation-related defect-free GaP/Si(100) heteroepitaxy via metal-organic chemical vapor deposition," *Appl. Phys. Lett.*, vol. 102, no. 14, pp. 17–21, 2013, doi: 10.1063/1.4801498.

[14] E. L. Warren, A. E. Kibbler, R. M. France, A. G. Norman, P. Stradins, and W. E. McMahon, "Growth of antiphase-domain-free GaP on Si substrates by metalorganic chemical vapor deposition using an *in situ* AsH_3 surface preparation," *Appl. Phys. Lett.*, vol. 107, no. 8, p. 082109, 2015, doi: 10.1063/1.4929714.

[15] J. M. Olson, M. M. Al-Jassim, A. Kibbler, and K. M. Jones, "MOCVD growth and characterization of GaP on Si," *J. Cryst. Growth*, vol. 77, no. 1–3, pp. 515–523, 1986, doi: 10.1016/0022-0248(86)90346-5.

[16] O. Supplie, M. M. May, G. Steinbach, O. Romanyuk, F. Grosse, A. Nägelein, P. Kleinschmidt, S. Brückner, and T. Hannappel, "Time-resolved in situ spectroscopy during formation of the GaP/Si(100) heterointerface," *J. Phys. Chem. Lett.*, vol. 6, no. 3, pp. 464–469, 2015, doi: 10.1021/jz502526e.

[17] J. Nishizawa, "Molecular Layer Epitaxy," *J. Electrochem. Soc.*, vol. 132, no. 5, p. 1197, May 1985, doi: 10.1149/1.2114058.

[18] K. J. Bachmann, "Heteroepitaxy of GaP on Si(100)," *J. Vac. Sci. Technol. B Microelectron. Nanom. Struct.*, vol. 14, no. 4, p. 3019, Jul. 1996, doi: 10.1116/1.589058.

[19] C. Ratcliff, T. J. Grassman, J. A. Carlin, and S. A. Ringel, "High temperature step-flow growth of gallium phosphide by molecular beam epitaxy and metalorganic chemical vapor deposition," *Appl. Phys. Lett.*, vol. 99, no. 14, 2011, doi: 10.1063/1.3644956.

[20] R. D. Hool, Y. Chai, Y. Sun, B. C. Eng, P. Dhingra, S. Fan, K. Nay Yaung, and M. L. Lee, "Relaxed GaP on Si with low threading dislocation density," *Appl. Phys. Lett.*, vol. 116, no. 4, 2020, doi: 10.1063/1.5141122.

[21] H. Strunk, W. Hagen, and E. Bauser, "Low-density dislocation arrays at heteroepitaxial Ge/GaAs-interfaces investigated by high voltage electron microscopy," *Appl. Phys.*, vol. 18, no. 1, pp. 67–75, 1979, doi: 10.1007/BF00935905.

[22] C. Ferrari, G. Rossetto, and E. A. Fitzgerald, "Misfit dislocation and threading dislocation distributions in InGaAs and GeSi/Si partially relaxed heterostructures," *Mater. Sci. Eng. B Solid-State Mater. Adv. Technol.*, vol. 91–92, pp. 437–440, 2002, doi: 10.1016/S0921-5107(01)00994-1.

[23] A. J. Wilkinson, "Observation of strain distributions in partially relaxed In0.2Ga0.8As on GaAs using electron channelling contrast imaging," *Philos. Mag. Lett.*, vol. 73, no. 6, pp. 337–344, Jun. 1996, doi: 10.1080/095008396180605.

[24] M. Feifel, J. Ohlmann, R. M. France, D. Lackner, and F. Dimroth, "Electron channeling contrast imaging investigation of stacking fault pyramids in GaP on Si nucleation layers," *J. Cryst. Growth*, vol. 532, no. July 2019, 2020, doi: 10.1016/j.jcrysgro.2019.125422.

[25] O. Romanyuk, O. Supplie, T. Susi, M. M. May, and T. Hannappel, "Ab initio density functional theory study on the atomic and electronic structure of GaP/Si(001) heterointerfaces," *Phys. Rev. B*, vol. 94, no. 15, pp. 1–9, 2016, doi: 10.1103/PhysRevB.94.155309.

[26] A. Beyer, A. Stegmüller, J. O. Oelerich, K. Jandieri, K. Werner, G. Mette, W. Stolz, S. D. Baranovskii, R. Tonner, and K. Volz, "Pyramidal Structure Formation at the Interface between III/V Semiconductors and Silicon," *Chem. Mater.*, vol. 28, no. 10, pp. 3265–3275, May 2016, doi: 10.1021/acs.chemmater.5b04896.

[27] I. Lucci *et al.*, "Universal description of III-V/Si epitaxial growth processes," *Phys. Rev. Mater.*, vol. 2, no. 6, pp. 1–6, 2018, doi: 10.1103/PhysRevMaterials.2.060401.

[28] S. D. Carnevale, J. I. Deitz, J. A. Carlin, Y. N. Picard, M. De Graef, S. A. Ringel, and T. J. Grassman, "Rapid misfit dislocation characterization in heteroepitaxial III-V/Si thin films by electron channeling contrast imaging," *Appl. Phys. Lett.*, vol. 104, no. 23, p. 232111, Jun. 2014, doi: 10.1063/1.4883371.

[29] S. D. Carnevale, J. I. Deitz, J. A. Carlin, Y. N. Picard, D. W. McComb, M. De Graef, S. A. Ringel, and T. J. Grassman, "Applications of electron channeling contrast imaging for the rapid characterization of extended defects in III-V/Si heterostructures," *IEEE J. Photovoltaics*, vol. 5, no. 2, pp. 676–682, 2015, doi: 10.1109/JPHOTOV.2014.2379111.

[30] A. N. Blumer, J. T. Boyer, J. I. Deitz, F. A. Rodriguez, and T. J. Grassman, "Quantitative Characterization of Misfit Dislocations at GaP/Si Heteroepitaxial Interfaces via Electron Channeling Contrast Imaging and Semi-Automated Image Analysis," *Microsc. Microanal.*, vol. 25, no. S2, pp. 202–203, Aug. 2019, doi: 10.1017/s1431927619001740.

[31] J. T. Boyer, A. N. Blumer, Z. H. Blumer, D. L. Lepkowski, and T. J. Grassman, "Reduced dislocation introduction in III-V/Si heterostructures with glide-enhancing compressively-strained superlattices," *Cryst. Growth Des.*, 2020.

[32] J. W. Matthews, S. Mader, and T. B. Light, "Accommodation of misfit across the interface between crystals of semiconducting elements or compounds," *J. Appl. Phys.*, vol. 41, no. 9, pp. 3800–3804, 1970, doi: 10.1063/1.1659510.

[33] M. Feifel, J. Ohlmann, J. Benick, T. Rachow, S. Janz, M. Hermle, F. Dimroth, A. Beyer, K. Volz, and D. Lackner, "MOVPE Grown Gallium Phosphide – Silicon Heterojunction Solar Cells," *IEEE J. photovoltaics*, vol. 7, no. 2, pp. 502–507, 2017, doi: 10.1109/JPHOTOV.2016.2642645.

[34] I. Gutierrez-Urrutia and D. Raabe, "Dislocation density measurement by electron channeling contrast imaging in a scanning electron microscope," *Scr. Mater.*, vol. 66, no. 6, pp. 343–346, Mar. 2012, doi: 10.1016/j.scriptamat.2011.11.027.

[35] B. Pang, I. P. Jones, Y.-L. Chiu, J. C. F. Millett, and G. Whiteman, "Electron channelling contrast imaging of dislocations in a conventional SEM," *Philos. Mag.*, vol. 97, no. 5, pp. 346–359, Feb. 2017, doi: 10.1080/14786435.2016.1262971.

[36] J. I. Deitz, S. D. Carnevale, S. A. Ringel, D. W. McComb, and T. J. Grassman, "Electron channeling contrast imaging for rapid iii-v heteroepitaxial characterization," *J. Vis. Exp.*, vol. 2015, no. 101, pp. 1–8, 2015, doi: 10.3791/52745.

[37] D. B. Williams and C. B. Carter, *Transmission Electron Microscopy*. Boston, MA: Springer US, 2009.

[38] A. J. Wilkinson and P. B. Hirsch, "Electron Diffraction Based Techniques in Scanning Electron Microscopy of Bulk Materials," vol. 4328, no. 97, 1997.

[39] A. J. Wilkinson, G. R. Anstis, J. T. Czernuszka, N. J. Long, P. B. Hirsch, G. R. Anstis, J. T. Czernuszka, N. J. Long, and P. B. Hirsch, "Electron channelling contrast imaging of interfacial defects in strained silicon-germanium layers on silicon," vol. 8610, 2006, doi: 10.1080/01418619308219357.

[40] H. Döscher, B. Kunert, A. Beyer, O. Supplie, K. Volz, W. Stolz, and T. Hannappel, "In situ antiphase domain

quantification applied on heteroepitaxial GaP growth on Si(100)," *J. Vac. Sci. Technol. B, Nanotechnol. Microelectron. Mater. Process. Meas. Phenom.*, vol. 28, no. 4, p. C5H1-C5H6, Jul. 2010, doi: 10.1116/1.3466529.

[41] I. Németh, B. Kunert, W. Stolz, and K. Volz, "Heteroepitaxy of GaP on Si: Correlation of morphology, anti-phase-domain structure and MOVPE growth conditions," *J. Cryst. Growth*, vol. 310, no. 7–9, pp. 1595–1601, 2008, doi: 10.1016/j.jcrysgro.2007.11.127.

[42] Y. G. Chai, Y. C. Pao, and T. Hierl, "Elimination of 'pair' defects from GaAs layers grown by molecular beam epitaxy," *Appl. Phys. Lett.*, vol. 47, no. 12, pp. 1327–1329, 1985, doi: 10.1063/1.96269.

[43] J. Faucher, T. Masuda, and M. L. Lee, "Initiation strategies for simultaneous control of antiphase domains and stacking faults in GaAs solar cells on Ge," *J. Vac. Sci. Technol. B, Nanotechnol. Microelectron. Mater. Process. Meas. Phenom.*, vol. 34, no. 4, p. 041203, 2016, doi: 10.1116/1.4945659.

[44] C. Frigeri, G. Attolini, C. Pelosi, and R. Gleichmann, "Stacking fault pyramids, island growth and misfit dislocations in InGaAs/InP heterostructures grown by vapour phase epitaxy," *Mater. Sci. Eng. B*, vol. 9, no. 1–3, pp. 115–119, Jul. 1991, doi: 10.1016/0921-5107(91)90158-R.

[45] N. Wang, I. K. Sou, and K. K. Fung, "Transmission electron microscopy study of stacking faults and the associated partial dislocations in pseudomorphic epilayers of ZnSe/GaAs(001)," *J. Appl. Phys.*, vol. 80, no. 9, pp. 5506–5508, 1996, doi: 10.1063/1.363482.

[46] S. D. Carnevale, J. I. Deitz, J. A. Carlin, Y. N. Picard, M. De Graef, S. A. Ringel, and T. J. Grassman, "Rapid characterization of extended defects in III–V/Si by electron channeling contrast imaging," in *2014 IEEE 40th Photovoltaic Specialist Conference (PVSC)*, Jun. 2014, pp. 2800–2803, doi: 10.1109/PVSC.2014.6925512.

[47] E. A. Fitzgerald, G. P. Watson, R. E. Proano, D. G. Ast, P. D. Kirchner, G. D. Pettit, and J. M. Woodall, "Nucleation mechanisms and the elimination of misfit dislocations at mismatched interfaces by reduction in growth area," *J. Appl. Phys.*, vol. 65, no. 6, pp. 2220–2237, Mar. 1989, doi: 10.1063/1.342834.

[48] Y. Takagi, Y. Furukawa, A. Wakahara, and H. Kan, "Lattice relaxation process and crystallographic tilt in GaP layers grown on misoriented Si(001) substrates by metalorganic vapor phase epitaxy," *J. Appl. Phys.*, vol. 107, no. 6, 2010, doi: 10.1063/1.3310479.

[49] F. K. LeGoues, P. M. Mooney, and J. Tersoff, "Measurement of the activation barrier to nucleation of dislocations in thin films," *Phys. Rev. Lett.*, vol. 71, no. 3, pp. 396–399, Jul. 1993, doi: 10.1103/PhysRevLett.71.396.

[50] E. A. Fitzgerald, A. Y. Kim, M. T. Currie, T. A. Langdo, G. Taraschi, and M. T. Bulsara, "Dislocation dynamics in relaxed graded composition semiconductors," *Mater. Sci. Eng. B Solid-State Mater. Adv. Technol.*, vol. 67, no. 1, pp. 53–61, 1999, doi: 10.1016/S0921-5107(99)00209-3.

[51] R. France, A. J. Ptak, C. S. Jiang, and S. P. Ahrenkiel, "Control of asymmetric strain relaxation in InGaAs grown by molecular-beam epitaxy," *J. Appl. Phys.*, vol. 107, no. 10, 2010, doi: 10.1063/1.3361533.

[52] C. Lynch, E. Chason, R. Beresford, L. B. Freund, K. Tetz, and K. W. Schwarz, "Limits of strain relaxation in InGaAs/GaAs probed in real time by in situ wafer curvature measurement," *J. Appl. Phys.*, vol. 98, no. 7, p. 073532, Oct. 2005, doi: 10.1063/1.2060947.

[53] L. B. Freund, "A criterion for arrest of a threading dislocation in a strained epitaxial layer due to an interface misfit dislocation in its path," *J. Appl. Phys.*, vol. 68, no. 5, pp. 2073–2080, 1990, doi: 10.1063/1.346560.

[54] U. Rossow, "Optical investigations of surface processes in GaP heteroepitaxy on silicon under pulsed chemical beam epitaxy conditions," *J. Vac. Sci. Technol. B Microelectron. Nanom. Struct.*, vol. 14, no. 4, p. 3040, Jul. 1996, doi: 10.1116/1.589061.

[55] A. Beyer, J. Ohlmann, S. Liebich, H. Heim, G. Witte, W. Stolz, K. Volz, A. Beyer, J. Ohlmann, S. Liebich,

H. Heim, G. Witte, W. Stolz, and K. Volz, "GaP heteroepitaxy on Si(001): Correlation of Si-surface structure, GaP growth conditions, and Si-III/V interface structure," *J. Appl. Phys.*, vol. 111, no. 8, p. 083534, 2012, doi: 10.1063/1.4706573.

[56] Y. Furukawa, H. Yonezu, K. Ojima, K. Samonji, Y. Fujimoto, K. Momose, and K. Aiki, "Control of N content of GaPN grown by molecular beam epitaxy and growth of GaPN lattice matched to Si(100) substrate," *Japanese J. Appl. Physics, Part 1 Regul. Pap. Short Notes Rev. Pap.*, vol. 41, no. 2 A, pp. 528–532, 2002, doi: 10.1143/jjap.41.528.

[57] V. Gottschalch, W. Heinig, E. Butter, G. Freydank, V. Gottscealch, W. Heinig, E. Butter, G. Freydank, D. Einflub, and G. Czochralski, "H_3P0_4 - Etching of {001}-Faces of InP, (GaIn)P, GaP, and Ga(AsP)," *Cryst. Res. Technol.,* vol. 14, no. 5, pp.563-569, 1979, doi: 10.1002/crat.19790140509.

[58] A. R. Laracuente and L. J. Whitman, "Step structure and surface morphology of hydrogen-terminated silicon: (0 0 1) to (1 1 4)," *Surf. Sci.*, vol. 545, no. 1–2, pp. 70–84, 2003, doi: 10.1016/j.susc.2003.08.038.

[59] G. Brocks, P. J. Kelly, and R. Car, "Binding and diffusion of a Si adatom on the Si(100) surface," *Phys. Rev. Lett.*, vol. 66, no. 13, pp. 1729–1732, Apr. 1991, doi: 10.1103/PhysRevLett.66.1729.

[60] S. Brückner, O. Supplie, A. Dobrich, P. Kleinschmidt, and T. Hannappel, "Control Over Dimer Orientations on Vicinal Si(100) Surfaces in Hydrogen Ambient: Kinetics Versus Energetics," *Phys. status solidi*, vol. 255, no. 4, p. 1700493, Apr. 2018, doi: 10.1002/pssb.201700493.

[61] A. Beyer and K. Volz, "Advanced Electron Microscopy for III/V on Silicon Integration," *Adv. Mater. Interfaces*, vol. 6, no. 12, pp. 1–15, 2019, doi: 10.1002/admi.201801951.

[62] A. Stegmüller, K. Werner, M. Reutzel, A. Beyer, P. Rosenow, U. Höfer, W. Stolz, K. Volz, M. Dürr, and R. Tonner, "Surface Chemistry of tert-Butylphosphine (TBP) on Si(001) in the Nucleation Phase of Thin-Film Growth," *Chem. - A Eur. J.*, vol. 22, no. 42, pp. 14920–14928, 2016, doi: 10.1002/chem.201602418.

[63] S. F. Bent, "Organic functionalization of group IV semiconductor surfaces: Principles, examples, applications, and prospects," *Surf. Sci.*, vol. 500, no. 1–3, pp. 879–903, 2002, doi: 10.1016/S0039-6028(01)01553-9.

[64] R. A. Wolkow, "Controlled molecular adsorption on silicon: Laying a foundation for molecular devices," *Annu. Rev. Phys. Chem.*, vol. 50, no. 100, pp. 413–441, 1999, doi: 10.1146/annurev.physchem.50.1.413.

[65] K. Werner, A. Beyer, J. O. Oelerich, S. D. Baranovskii, W. Stolz, and K. Volz, "Structural characteristics of gallium metal deposited on Si (0 0 1) by MOCVD," *J. Cryst. Growth*, vol. 405, pp. 102–109, 2014, doi: 10.1016/j.jcrysgro.2014.07.045.

[66] P. Kumar and C. H. Patterson, "Dielectric Anisotropy of the GaP/Si(100) Interface from First-Principles Theory," *Phys. Rev. Lett.*, vol. 118, no. 23, p. 237403, Jun. 2017, doi: 10.1103/PhysRevLett.118.237403.

[67] A. Lenz, O. Supplie, E. Lenz, P. Kleinschmidt, and T. Hannappel, "Interface of GaP/Si(001) and antiphase boundary facet-type determination," *J. Appl. Phys.*, vol. 125, no. 4, 2019, doi: 10.1063/1.5080547.

[68] K. Sumino and I. Yonenaga, "Interactions of impurities with dislocations: Mechanical effects," *Solid State Phenom.*, vol. 85–86, pp. 145–176, 2002, doi: 10.4028/www.scientific.net/ssp.85-86.145.

Highlights

- Statistically relevant ECCI-based method for quantitative defect dynamics analysis.
- Systematic correlation of GaP/Si MOCVD nucleation processes with defect evolution.
- Two order-of-magnitude reduction in GaP/Si TDD with improved nucleation process.
- Stacking fault pyramid density correlated with, but not driver of, TDD.

CRediT Author Statement

J. T. Boyer: Conceptualization, Methodology, Formal analysis, Investigation, Writing - original draft. **A. N. Blumer:** Investigation, Methodology, Formal analysis, Writing - review & editing. **Z. H. Blumer:** Investigation, Writing - review & editing. **D. L. Lepkowski:** Investigation, Writing - review & editing. **T. J. Grassman:** Conceptualization, Methodology, Supervision, Project administration, Funding acquisition, Writing - review & editing.

Declaration of interests

☒ The authors declare that they have no known competing financial interests or personal relationships that could have appeared to influence the work reported in this paper.

☐The authors declare the following financial interests/personal relationships which may be considered as potential competing interests: